Lipid membranes supported by polydimethylsiloxane substrates with designed geometry

Rinaldin, M.; Haaf, S.L.D. ten; Vegter, E.J.R.; Wel, C.M. van der; Fonda, P.; Giomi, L.; Kraft, D.J.

Volume 20
Number 37
7 October 2024
Pages 7335–7548

Soft Matter

rsc.li/soft-matter-journal

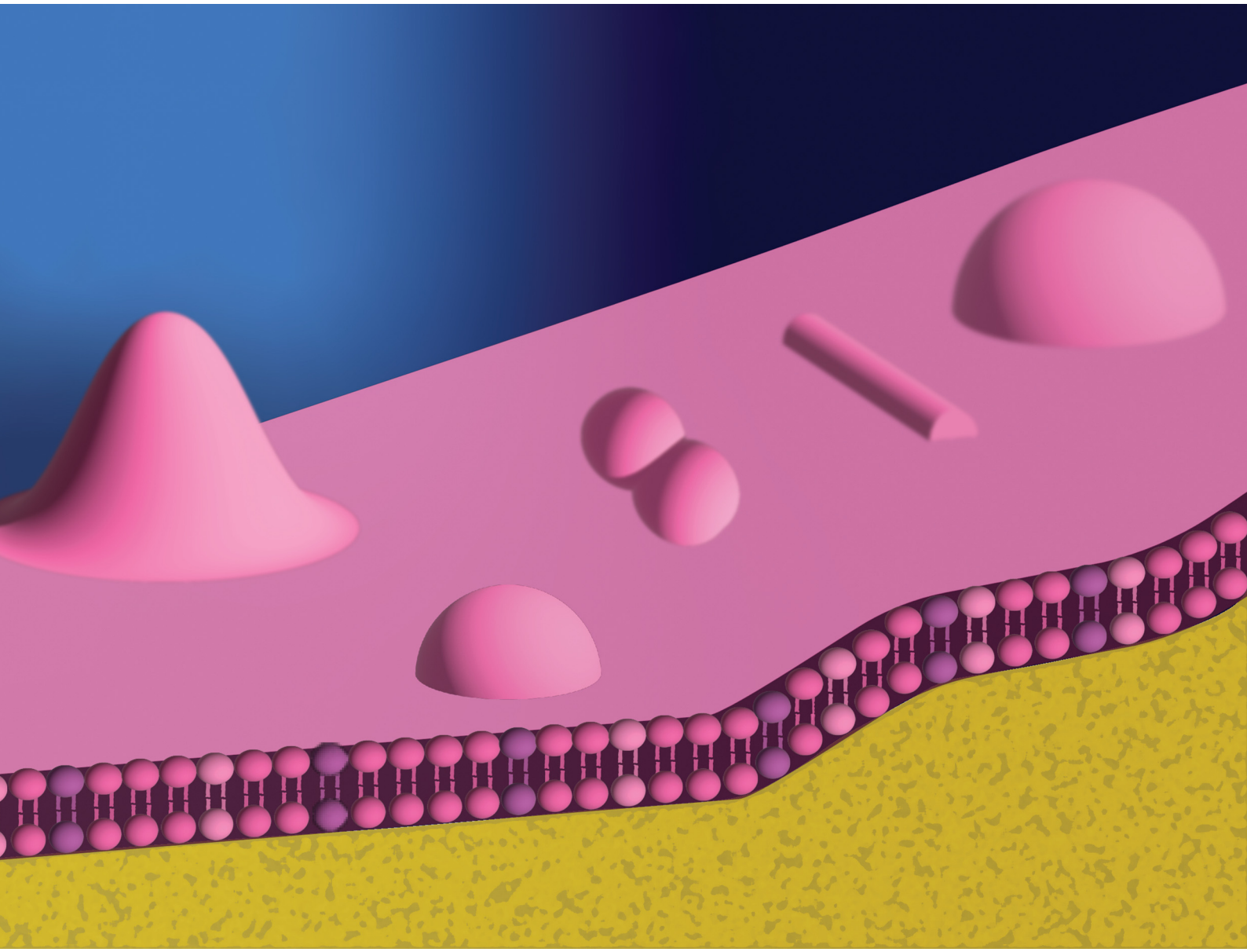

ISSN 1744-6848

ROYAL SOCIETY OF CHEMISTRY

PAPER
Melissa Rinaldin, Daniela J. Kraft *et al.*
Lipid membranes supported by polydimethylsiloxane substrates with designed geometry

Soft Matter

PAPER

View Article Online
View Journal | View Issue

Cite this: *Soft Matter*, 2024, **20**, 7379

Lipid membranes supported by polydimethylsiloxane substrates with designed geometry†

Melissa Rinaldin, ‡*[ab] Sebastiaan L. D. ten Haaf,[a] Ernst J. Vegter,[a] Casper van der Wel,[a] Piermarco Fonda,[b] Luca Giomi [b] and Daniela J. Kraft *[a]

Received 2nd April 2024,
Accepted 30th June 2024

DOI: 10.1039/d4sm00380b

rsc.li/soft-matter-journal

The membrane curvature of cells and intracellular compartments continuously adapts to enable cells to perform vital functions, from cell division to signal trafficking. Understanding how membrane geometry affects these processes *in vivo* is challenging because of the biochemical and geometrical complexity as well as the short time and small length scales involved in cellular processes. By contrast, *in vitro* model membranes with engineered curvature would provide a versatile platform for this investigation and applications to biosensing and biocomputing. Here, we present a strategy that allows fabrication of lipid membranes with designed shape by combining 3D micro-printing and replica-molding lithography with polydimethylsiloxane to create curved micrometer-sized scaffolds with virtually any geometry. The resulting supported lipid membranes are homogeneous and fluid. We demonstrate the versatility of the system by fabricating structures of interesting combinations of mean and Gaussian curvature. We study the lateral phase separation and how local curvature influences the effective diffusion coefficient. Overall, we offer a bio-compatible platform for understanding curvature-dependent cellular processes and developing programmable bio-interfaces for living cells and nanostructures.

Introduction

Controlling the geometry of *in vitro* lipid membranes is critical for advancements in cellular biology and bioengineering.[1–3] Current approaches to control the shape of model membranes consist of manipulating lipid vesicles *in situ*[4,5] or creating supported lipid bilayers.[6] These techniques, however, only give access to a limited range of shapes, which makes them unsuitable for investigating curvature-dependent cellular processes, such as intracellular signaling,[7,8] applications such as live-cell manipulation[9–12] and DNA origami circuit construction.[13–15] Moreover, most efforts until now have been directed to the fabrication of grids,[6,16] corrugate surfaces,[16] and buds.[17] Most recently, 3D printing has been used to create surfaces of any shape that can be later functionalized for lipid coating.[18] However, current strategies depend on the properties of commercial photoresists, do not allow for substrate flexibility, and require high manufacturing time because of micro-printing every single substrate.

To overcome these limitations, here we present a strategy based on membrane-supporting microstructures created with 3D object rational design, direct laser writing, and subsequent replica-molding with polydimethylsiloxane (PDMS). The versatile workflow specific to 3D micro-printing allows to create lipid membranes of potentially arbitrarily any geometry. The PDMS used in the replica-molding step enables the crucial homogeneity and fluidity of the membrane as well as creating multiple substrates from one print. Moreover, PDMS can be used at different temperatures, is transparent, low-cost, possesses low chemical reactivity, is biocompatible,[19] deformable, and has been previously used for lipid membrane coating.[20,21] The elastic modulus of PDMS (E) can be adjusted to mimic a wide range of stiffnesses, from about 4 kPa to 10 MPa,[19,21,22] simply by changing the composition and without affecting the surface properties. These stiffnesses are in the range measured in biological environments that interact with lipid membranes, such as cell to cell contacts in T cells ($E \sim 4$ kPa),[21] the actomyosin cortex ($E \sim 42$ kPa),[23] and the extracellular matrix ($E \sim 1$ MPa).[22]

The combination of tunability of the elastic modulus with microprinting allows to model membrane curvature-inducing mechanisms, for example the microscopic curvature generated

[a] *Leiden Institute of Physics, University of Leiden, 2300 RA Leiden, The Netherlands. E-mail: kraft@physics.leidenuniv.nl*
[b] *Instituut-Lorentz, Universiteit Leiden, Leiden, 2300 RA, The Netherlands*

† Electronic supplementary information (ESI) available. See DOI: https://doi.org/10.1039/d4sm00380b

‡ Current affiliation: Physics of Life Excellence Cluster, TU Dresden, 01307, Dresden, E-mail: melissa.rinaldin@tu-dresden.de

by lamellipodia of a measured elastic modulus equal to $E \sim 34$ kPa.[24]

Our method allows programming membrane curvature with extensive design freedom and high spatial resolution, and hence could provide a versatile platform for investigating biological processes associated with distinct membrane geometries and for engineering novel bio-interfaces.

Experimental

Reagents

The lipids (Δ9-*cis*)1,2-dioleoyl-*sn-glycero*-3-phos-phocholine (DOPC), 1-palmitoyl-2-oleoyl-*sn-glycero*-3-phosphocholine (POPC), porcine brain sphingomyelin(BSM), ovine wool cholesterol (Chol), 1,2-dioleoyl-*sn-glycero*-3-phosphoethanolamine-*N*-[methoxy(polyethyleneglycol)-2000] (DOPE-PEG(2000)), and L-α-phosphatidylethanolamine-*N*-(DOPE lissamine rhodamine B sulfonyl) were purchased from Avanti Polar Lipids and stored at −20 °C. Propylene glycol monomethyl ether acetate (PGMA, ≥99.5%) and trichloro(1*H*,1*H*,2*H*,2*H*-perfluorooctyl) silane (≥97%) were purchased from Sigma-Aldrich. 2-Propanol (≥99.6%) was purchased from Honeywell. Silcon wafers of 10 cm diameter, 1 Ω cm resistivity, and 525 μm thickness were purchased from Siegert Wafer. IP-S photoresist was purchased by Nanoscribe GmbH and Ormocomp by Microresist. Polymethylsiloxane (PDMS) was purchased from Dow Corning. 4-(2-hydroxyethyl)-1-piperazine- ethanesulfonic acid (HEPES, ≥ 99.5%) and calcium chloride ($CaCl_2$, calciumchlorid dihydrat, ≥ 99%) were purchased from Carl Roth. Sodium chloride (NaCl, extrapure) and dipotassium phosphate (K_2HPO_4 ≥ 99%) was purchased from Sigma Aldrich. Magnesium chloride ($MgCl_2$, for analysis) was purchased from Merck.

Fabrication of solid substrates

Microstructures for membrane formation were prepared by PDMS replica-molding from 3D printed molds. The 3D structure of the molds was designed using the software Autodesk Inventor (Autodesk) and processed with the program Describe (Nanoscribe GmbH) to obtain a mesh of points suitable for micro-printing. Subsequently, the molds were fabricated by two-photon lithography using a commercial 3D microprinter (Nanoscribe GmbH, Photonics Professional GT). The photoresist (IP-S, Nanoscribe GmbH) was employed as a pre-polymer. The photoresist was polymerized by exposure to a 780 nm laser focused by a 63× objective (NA = 1.48, Carl Zeiss) directly in contact with the photoresist. Slice by slice, small volumes (400 μm × 400 μm × 100 μm) were exposed using galvanic mirrors and stitched together by moving a mechanical stage. The laser power used was 30 mW. The unpolymerized resist was removed in a bath with PGMA for 15 minutes and rinsed with 2-propanol. The fabrication and the cleaning of the molds were performed under yellow light (λ = 577–597 nm) to prevent spontaneous polymerization. The molds were salinized with trichloro(1*H*,1*H*,2*H*,2*H*-perfluorooctyl) silane under vacuum for 2 hours to prevent irreversible sticking of PDMS on the surface. A PDMS pre-polymer mixture was prepared from a 1 : 10 elastomer: crosslinker mixture by weight.[25] It was degassed for 30 minutes under vacuum, poured onto the molds, and further degassed for 2 hours to eliminate any bubbles present, which could affect the shape of the microstructures. Then, the microstructures were cured with temperature for 2 hours at 100 °C for polymerization. Finally, the cured structures were peeled from the molds. Before being used for lipid coating, the microstructures were washed for 10 minutes by sequential sonication in acetone, ethanol, and MilliQ water. The microstructures were dried in an oven (and treated with UV/ozone for one hour to fully hydrophilize the surface. The resulting PDMS microstructures were used immediately for the lipid coating to avoid hydrophobization of PDMS.

Membrane formation

Membranes were formed by deposition of small unilamellar vesicles (SUVs) obtained *via* extrusion at high pressure. A mixture of lipids (500 μg) in chloroform (94.8% DOPC, 5% DOPE-PEG (2000), and 0.2% DOPE-rhodamine, mole ratio) was prepared for all experiments apart from the ones in which we studied phase separation. For phase separation experiments we used 19.8% POPC, 0.2% DOPE-rhodamine, 5% DOPE-PEG (2000), 50%BSM, 25% Chol molar ratio. The phase separation composition was chosen based on previously obtained phase diagrams[26,27] to be a molar ratio of 1 : 2 : 1 POPC : BSM : Chol. To incorporate DOPE-PEG (2000) and DOPE-rhodamine which are low temperature melting lipids, we reduced the concentration of POPC to maintain the overall 25% mole fraction of low-temperature melting lipids. The chloroform was evaporated in a vacuum chamber for 2 hours. The lipids were dispersed in HEPES buffer and assembled in multilamellar vesicles during 30 minutes of vortexing. HEPES buffer was made with 115 mM NaCl, 1.2 mM $CaCl_2$, 1.2 mM $MgCl_2$, 2.4 mM K_2HPO_4 and 20 mM HEPES. After mixing with fresh milliQ water, the pH was adjusted to 7.4 using NaOH. The solution was extruded 21 times with a mini-extruder (Avanti Polar Lipids) equipped with two 250 μL gas-tight syringes (Hamilton), two drain discs, and one nucleopore track-etch membrane with pores of 0.05 μm diameter (Whatman). 50 μL of SUV solution diluted in 1 mL of HEPES buffer was slowly flushed into a flow cell (Fig. S2, ESI†) containing the PDMS microstructures and incubated for 1 hour. This amount of SUVs was chosen to ensure that there were enough lipids to cover the surface. Finally, the flow cell was flushed with HEPES buffer to remove excess SUVs.

Membrane characterization and Fluorescence recovery after photobleaching (FRAP) measurements

The samples were imaged at room temperature with an inverted confocal microscope (Nikon Eclipse Ti-E) equipped with a Nikon A1R confocal scan head with Galvano and resonant scanning mirrors. 20× and 60× air objectives (NA = 0.75 and 0.7, respectively) were used. A 561 nm laser was used to excite the rhodamine dye. The laser was passed through a quarter-wave plate to avoid polarization of the dyes. The emitted light was separated using a 565–625 nm filter. Three-dimensional image stacks were

acquired by scanning the sample in the *z*-direction with a MCL Nano-drive stage and reconstructed with Nikon AR software. During the imaging, the microstructures were positioned upside down in the flow chamber to avoid diffraction effects. FRAP experiments were performed using the Nikon AR software and the microscope described above operated in the non-resonant mode together with a 561 nm laser for bleaching. For flat substrates, the half domes in Fig. 2e and f, a circular area to bleach was chosen equal to 5 μm, 3.5 μm, 1 and 2 μm, respectively. The time and power of the laser was adjusted to ensure that bleaching an area of a size close to what was chosen. The recovery signal was first analysed by integrating the intensity of the bleached and reference areas over time by using ImageJ. Then these quantities were analysed using a custom-made Python software. Calculation of the diffusion coefficient from the FRAP data is discussed in the ESI,† in Sections 1 and 2, for the planar and spherical case, respectively. For the FRAP data of Fig. 2f, at least 7 measurements for each radius were averaged and the error associated is equal to the standard deviation.

Results and discussion

We illustrate our strategy for creating supported lipid membranes with designed shape in Fig. 1a. First, we designed the desired support structure by creating 3D molds of the inverted shape using AutoCAD Inventor. We fabricated the molds by 3D micro-printing *via* two-photon polymerization using a commercially available printer (Fig. 1a, step 1). To achieve high spatial resolution, arrays of the molds were printed onto silicon wafers using commercial photoresist and 63× oil-immersion objective (Zeiss, NA = 1.48). Specifically, we used the photoresist IP-S (Nanoscribe), however other photoresists could be used in principle as well. A femtosecond laser traced the mold shape through galvanic mirrors, and a mechanical stage controlled with a piezoelectric actuator allowed displacing the substrate to create larger structures. The accessible size range, from hundreds of nanometers to millimeters, and spatial accuracy down to 100 nm can only be obtained through 3D direct laser writing. The molds were finalized by developing the printed resist in a

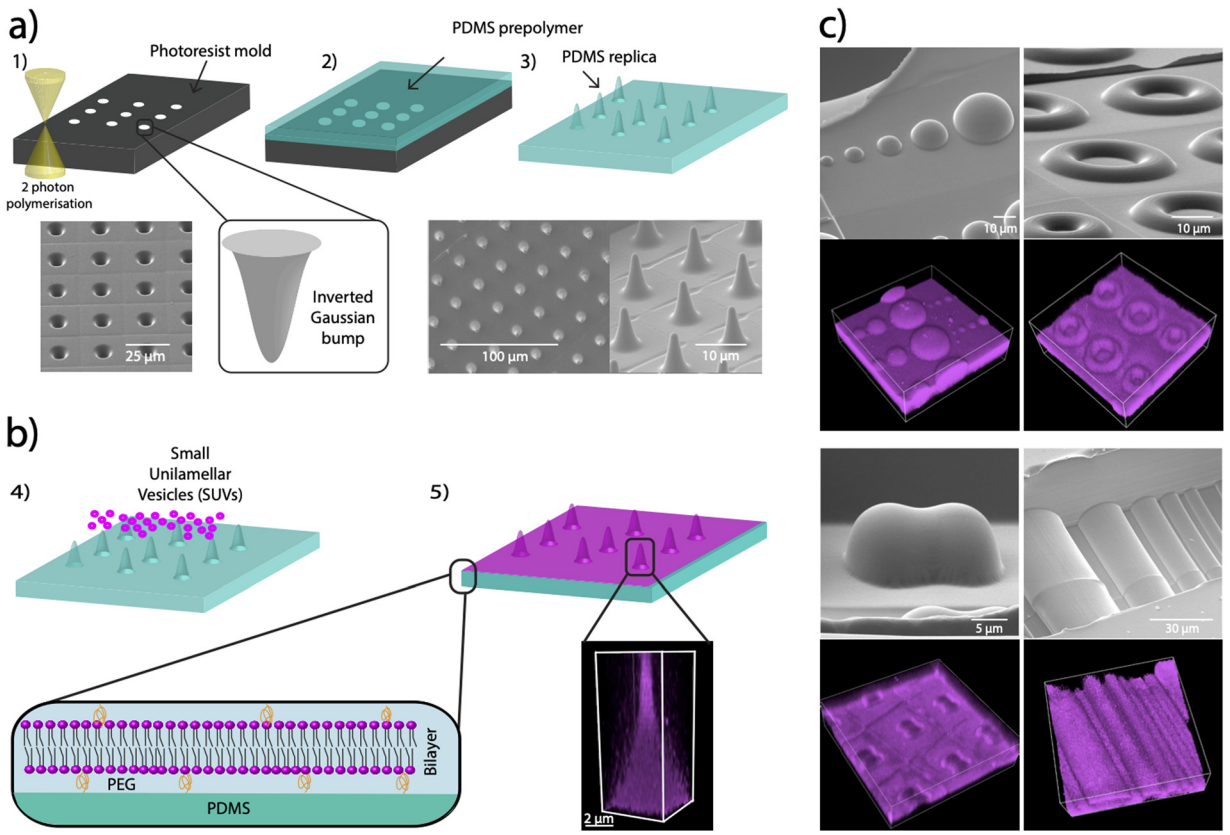

Fig. 1 Fabrication of supported lipid membranes with designed shape. (a) Microstructures fabrication. Step (1) Molds of Gaussian bumps are fabricated by two-photon polymerization. Step (2) PDMS pre-polymer is poured over the developed microprinted molds and cured. Step (3) The resulting microstructures are peeled from the molds. Scanning electron microscopy (SEM) images of the PDMS Gaussian bumps (right) and their mold counterparts (left) are shown in the bottom row. (b) Membrane formation. Step (4–5) The microstructures are functionalized with a lipid membrane by deposition of small unilamellar vesicles (SUVs). The lipid composition is 94.8% DOPC, 0.2% DOPE Rhodamine, and 5% DOPE-PEG(2000) mole ratio. On the bottom-left, a close-up schematic view of the membrane supported on a PDMS substrate is shown. PEGylated lipids DOPE-PEG (2000) (orange) are used to increase the water layer between the PDMS substrate and the membrane and therefore increase the fluidity of the membrane (magenta). On the bottom-right, a 3D fluorescence microscopy image of one of the Gaussian bumps is reported. (c) Membranes with designed shape. SEM images of PDMS microstructures of with half-spherical and half-toroidal (top), and half-dumbbell and half-cylindrical shape (bottom) along with fluorescence volume reconstruction of the membranes.

solution of propyleneglycolmethyletheracetate (PGMA) under UV light. Subsequently, to create the scaffold, a solution of PDMS pre-polymer was poured over the molds and cured at a temperature of 100 °C for 2 hours. The obtained polymerized PDMS has a Young's modulus of 2.5 ± 0.1 MPa[25] (Fig. 1a, step 2). This choice of Young's modulus was based on previous work,[25] however we note that the material properties of the PDMS can be tuned by simply changing the mixing ratio and temperature. In principle, PDMS substrates could be prepared even with a Young modulus equal to the one of current commercial PDMS photoresists used for 3D printing (Young's modulus of 15.3 MPa).[28] Finally, the polymerized PDMS was peeled from the molds to obtain the substrate patterned with an array of the desired support structure, for example Gaussian bumps (Fig. 1a, step 3). The 3D printed mold has a resolution set by the printing accuracy which in our case is 100 nm. This results in substrates that possess surface roughness at that length scale. After molding however, the PDMS structures present a smoother surface (Fig. S3, ESI†) with no visible roughness. Moreover, by using PDMS we can tune the stiffness of the substrate by simple changes of the ratio of the components.

This replica molding with PDMS was a critical step to fabricate substrates suitable for lipid functionalization. Indeed, lipid coating of substrates made of IP-S or Ormocomp photoresists led to homogeneous but only partially fluid membranes, with significantly slower diffusion constants (D_{FRAP}, IP-S = 0.2 ± 2.0 μm^2 s^{-1} and D_{FRAP}, Ormocomp = 0.40 ± 0.01 μm^2 s^{-1} consistent with previous work[18]) and recovery percentages of 28% and 60%, respectively, as measured by fluorescent recovery after photobleaching (FRAP), see Fig. S1 and Table S1, ESI†). Finally, we coated the PDMS supports with a lipid membrane *via* vesicle deposition. To prevent monolayer formation,[29] we hydrophilized the PDMS surface by thorough cleaning with sequential sonication in acetone, ethanol, and MilliQ water and UV/ozone treatment. Then, we positioned the PDMS microstructures in a flow cell where a solution of small unilamellar vesicles (SUVs) made of a mixture of lipids consisting of 94.8% DOPC, 0.2% DOPE Rhodamine, and 5% DOPE-PEG (2000) mole ratio was flown in (Fig. 1b, step 4). In comparison, lipid diffusion on PDMS substrates was measured to be significantly higher than on Ormocomp or IP-S (D_{FRAP}= 1.3 ± 0.1 μm^2 s^{-1}), which is consistent with the literature.[30] However, it is still slower than typical values that we measured for glass (D_{FRAP}= 4.1 ± 0.1 μm^2 s^{-1}). The use of DOPE-PEG (2000) increases the distance between lipids and substrate and hence it preserves membrane fluidity.[27,31] The fluidity through DOPE-PEG (2000) is crucial for studying diffusion and phase separation as we will do below, however we note that this might hamper additional functionalization, for example of proteins. Specifically, it has been shown that if PEG-ylated lipids are used in high concentrations and high molecular weights, they can be in the brush state and affect the absorption of plasma proteins.[32,33] The amount and size of PEG we use in our study, however, is such that the polymers are in the mushroom state[32] and should allow protein binding with the bilayer. DOPE Rhodamine allows for imaging the membrane using confocal microscopy. After one hour of incubation, the PDMS substrate was fully covered by the membrane and formed a stable bilayer for over 15 hours. Using the bilayer for longer time scales is not recommended as it is expected to degrade and form holes.[34,35] The supported lipid membrane follows the geometry of the mold perfectly within the resolution of confocal microscopy, and likely even down to the nanoscale precision,as previously shown using this technique on nanoparticles[36] (Fig. 1b, step 5).

The versatility of rational 3D micro-printing design allows to straightforwardly create a library of shapes and mimic the myriad of conformations taken on by cellular membranes.[9] The precise design allows to study the role of local curvature in physical processes, such as diffusion, phase separation, and lateral organization of proteins on curved membranes. To demonstrate this versatility, in Fig. 1c, we report examples of hemispherical, half-toroidal, -dumbbell, -cylindrical microstructures, with and without the lipid coating. This selection of shapes allows us to manipulate the local curvatures of the membrane. The hemisphere has homogeneous mean and Gaussian curvatures. The half-torus has a varying mean and Gaussian curvature (positive inside and negative outside), while cylinders have homogeneous mean curvature and vanishing Gaussian curvature. Half-dumbbells contain valley-like features which are reminiscent of size-controlled necks in supported lipid vesicles (SLVs), which have been used to measure Gaussian rigidity difference in multicomponent membranes.[27] Furthermore, similar minimal neck-like shapes could be used for more precise measurements of the saddle splay modulus *via* flickering interface analysis.[37]

To functionalize membranes with biomolecules and nanostructures,[11] the supported membrane must be homogeneous and fluid.[31] We tested whether our supported membranes feature homogeneity by examining the fluorescence intensity of the bilayer on 3 × 3 array of 10 μm-diameter hemispheres. We found that the intensity is homogenous across the membrane and independent of the curvature of the substrate (Fig. 2a). We note that scattering renders the bilayer to appear thicker that it is. The fluorescence intensity along a line taken on the top of a hemisphere randomly fluctuates around its mean value, indicating that the membrane is homogeneous (Fig. 2b and c). To measure membrane fluidity, we performed FRAP experiments (Fig. 2d and e). We simultaneously bleached a circular area around the top of 8 hemispheres, and observed complete recovery of the intensity, see Fig. 2d. Indeed, the normalized intensity for each sphere which includes a correction for imaging photobleaching, follows roughly the same exponential curve, with an average half time of $\tau_{1/2}$ = 4.8 s and average mobile lipid fraction 93% (Fig. 2e). See ESI,† Table S2 for details on the fit parameter.

The combination of designed geometry, preserved homogeneity and fluidity makes our protocol a powerful platform for quantitative studies on geometry-dependent effects on model membranes. To demonstrate this, we quantify the impact of curvature on the FRAP diffusion coefficient.[38–41] We performed FRAP experiments at the top of hemispheres of five different

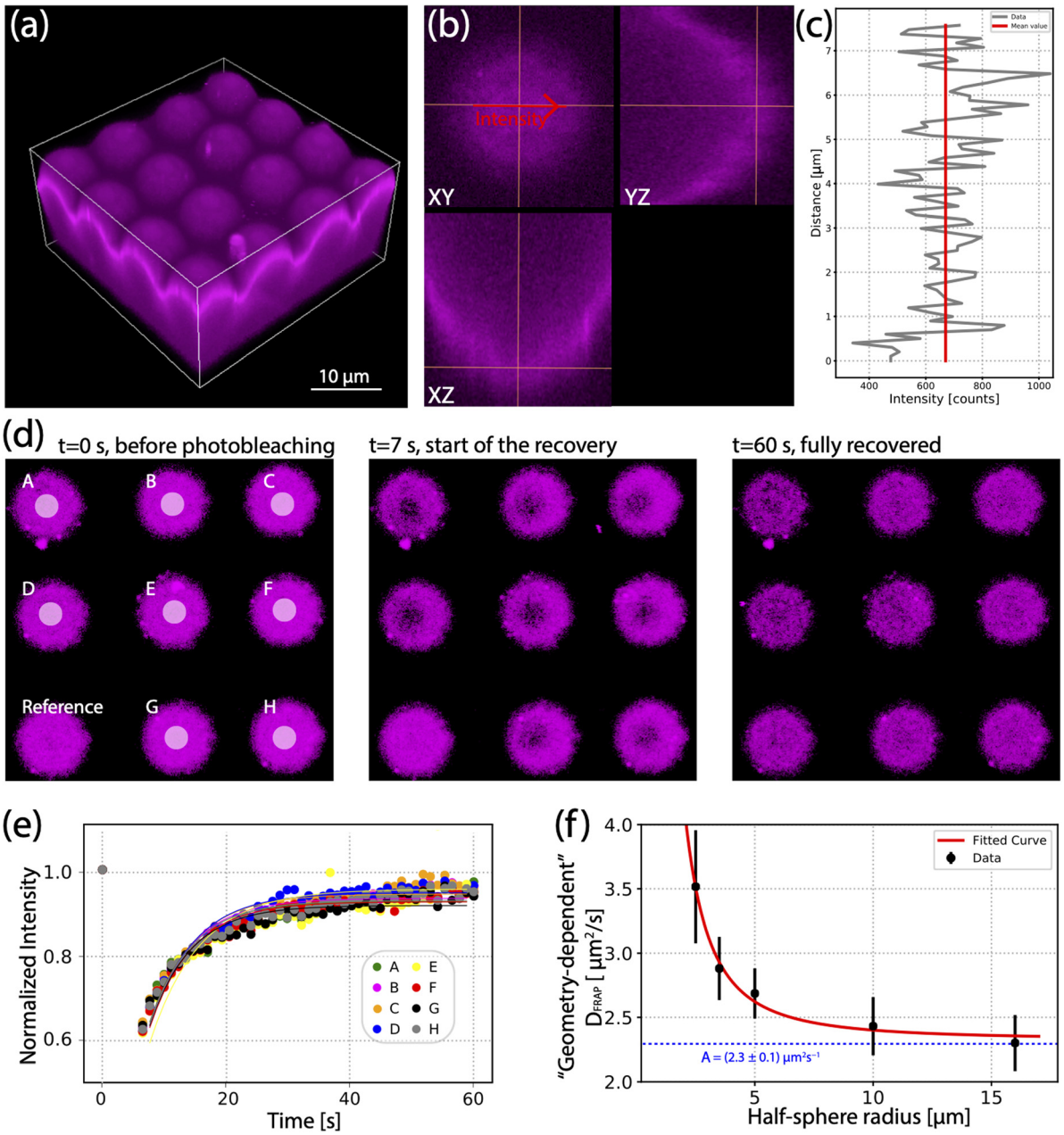

Fig. 2 Membrane homogeneity and fluidity. (a) 3D reconstruction of a membrane on half-spherical microstructures of 5 µm radius. (b) XY, YZ, and XZ projections of the membrane on the top of one hemisphere. The intensity of the fluorescent signal along the grey axis is plotted in (c) which shows the intensity fluctuating around an average value, indicating that the membrane is homogeneous. (d) FRAP experiments on the top of eight half-spherical membranes. The bleaching areas (white disks) are labelled with letters from A to H. From left to right, the stages before and after bleaching, as well as at the end of the recovery are reported. A reference area is used to correct for bleaching due to the imaging. (e) Experimental data (cirlces) and fits (lines) of the FRAP experiments. The intensities recover almost completely. (f) FRAP "geometry dependent" diffusion coefficient as a function of the radius of the hemispheres, with a least-square fit using $D_{FRAP} = A + B/R^2$, where $A = (2.3 \pm 0.1)$ µm^2 s^{-1} which is an estimate of the value of the diffusion coefficient on flat substrates, and $B = (7.4 \pm 0.2$ µm^4 s$^{-1})$.

radii and measured the FRAP diffusion coefficient (D_{FRAP}). To account for the fact that the bleached area is a spherical cap, we modified the expression of D_{FRAP} given by Axelrod *et al.*[42] by using the surface area of a spherical cap instead of a flat disk (see ESI,† Section III). We observe in Fig. 2f that D_{FRAP} depends on the substrate shape, and in particular that D_{FRAP} is inversely proportional to the square of the radius of the half-spherical substrate. While the actual diffusion coefficient of the lipids is not affected by the curvature, the radius dependence of D_{FRAP} captures the collective effect of the half-spherical geometry on the mean square displacement (MSD) of the single lipids. Indeed, by expressing the MSD of particles diffusing on a sphere[43] in terms of a "curvature-dependent" diffusion coefficient, the radius dependence of D_{FRAP} found in Fig. 2f and an

estimation of the diffusion coefficient on the flat PDMS can be recovered (see ESI,† Section III).

Homogenous fluid lipid membranes scaffolded onto designed surfaces offer a compelling opportunity to precisely engineer the formation of local heterogeneities *via* liquid–liquid phase separation. For specific temperatures and lipid compositions, artificial lipid membranes undergo liquid–liquid phase separation from one homogenous liquid phase into two distinct liquid phases: a more rigid, liquid-ordered phase (LO), and a softer, liquid-disordered (LD), phase.[44] In the presence of curvature, the LO and LD domains organize into specific patterns dictated by the curvature of the underlying substrate.[44–46] We induced lipid phase separation in our set-up by using a lipid mixture containing cholesterol, sphingomyelin, POPC in mole ratio equal to 25 : 50 : 25, where the POPC phase contained DOPE-PEG and DOPE-rhodamine for enhancing fluidity and enabling imaging. Moreover, the SUV formation and lipid coating were performed by setting the temperature of the oven to 70 °C, *i.e.* well above the critical transition temperature, which is expected to be between 35 °C and 45 °C, to ensure mixing of the lipids.[47] After the lipid coating, the membrane was cooled to 25 °C at a rate of 0.04 °C min^{-1}. The controlled gradual cooling was performed using a programmable oven (UFE, Memmert) was critical to allow the lipid domains to reach a phase-separated equilibrium state and avoid kinetically arrested configurations.[48]

In Fig. 3a we show that we achieved lateral phase separation on half-spherical microstructures of varying radius. The LD phase was labelled in magenta using 0.2%mol DOPE-rhodamine and the circular LO domains were unlabeled and hence appear dark (Fig. 3a). The circular domains resemble domains observed in previous studies of phase-separated membranes in GUVs[49] and are strikingly different from the kinetically arrested irregular patterns of small spots found for lipid mixtures that do not phase separate.[30,48,50]

While on the flat parts of the membrane the LO domains are spatially randomly distributed and feature similar sizes, on the hemispheres the occurrence and size of the LO domains are influenced by the substrate curvature. This can be seen in Fig. 3c, where we report top views of half-spherical membranes as sketched in Fig. 3b. On the smallest hemisphere of radius 2.5 μm there are no observable LO domains. By increasing the radius, more numerous and larger LO domains are present on the half spheres because of the larger surface available and the preference of LO domains for less curved regions.[44–46] The

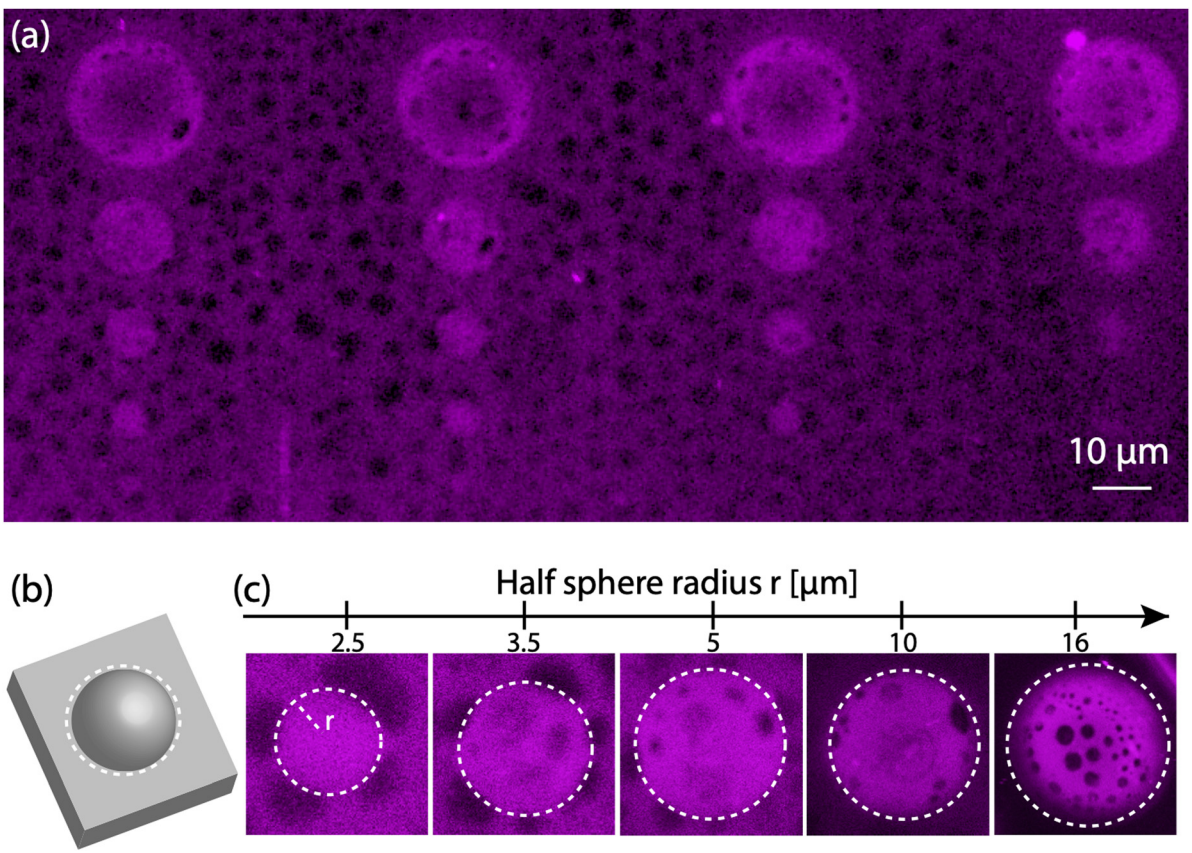

Fig. 3 Phase-separated membrane on half-spherical microstructures of varying radius. (a) Fluorescence microscopy image of a phase-separated membrane on half-spherical microstructures. LD phase is labelled by DOPE-rhodamine (magenta). Circular LO domains are visible both on the flat substrate and the half-spherical structures. (b) Schematic view of the half spheres from the top, as shown in (c). Top views of the phase-separated membranes on hemispheres with 2.5, 3.5, 5, 10, and 16 μm radius. The LD phase is shown in magenta. The boundary of the hemispheres is shown by dotted white circles. For the smallest radius, LO domains are depleted from the hemisphere. As the radius increases, or the curvature decreases, the amount of LO domains on the hemispheres increases indicating a preference for the LO domains for less curved regions.

presence of multiple circular domains indicates that the system has locally, and not globally reached equilibrium. Achieving phase separation in supported lipid bilayers is generally challenging. The resulting inhomogeneous spatial distribution of lipid domains suggests that we can use this technique for fabricating curved substrates with chemically distinct domains which can be functionalized at will with biomolecules and nanoparticles, for example through biotin–streptavidin binding to (un)saturated lipids.

Conclusions

In conclusion, we presented a novel approach to fabricating a plethora of homogenous and fluid curved lipid membranes in a precise and programmable fashion. We exploited the rational design capabilities of 3D micro-printing to obtain specific anisotropic structures and used the biocompatibility of PDMS to achieve homogeneous and fluid membranes which can feature chemically distinct domains upon using a ternary lipid mixture.

We limited our study to substrates with a fixed elastic modulus of the order of a few MPa and microscopic curvature. However, since the elasticity of PDMS can be tuned without changing its surface properties, we expect that our approach could be extended to substrates with lower elastic moduli and nanoscopic curvatures.

Our membranes with designed shapes are a powerful platform for unravelling curvature-dependent biological processes in membranes, such as sorting of proteins and lipids in signal trafficking.[1,2,51] Moreover, our strategy opens up new possibilities in bio-engineering and material science. Specifically, the development of synthetic platforms to impose curvature on living cells for mechanobiology,[9–12] immunology experiments[21] and bottom-up construction of complex nanostructures of DNA-origami building blocks.[13–15]

Author contributions

Conceptualization: MR, DJK, LG. investigation: MR, SLDtH, EJV, CvdW, and DJK. formal analysis: MR, PF, LG. supervision: DJK and LG. Writing the original draft: MR and DJK. Writing – reviewing – editing: MR, PF, LG. funding: DJK and LG.

Data availability

Data and code of this manuscript will be made available upon request. The files for the blueprint of the flow cell are included in this publication as ESI.†

Conflicts of interest

There are no conflicts to declare.

Acknowledgements

This work was supported by the Netherlands Organization for Scientific Research (NWO/OCW), as part of the Frontiers of Nanoscience program. We thank Joseph Salaris for preliminary experiments, Jeroen Mesman for the fabrication of the flow cell for lipid functionalization, and Rachel Doherty for the electron microscopy imaging.

Notes and references

1 H. T. McMahon and J. L. Gallop, *Nature*, 2005, **438**, 590–596.
2 H. T. McMahon and E. Boucrot, *J. Cell Sci.*, 2015, **128**, 1065–1070.
3 C.-H. Yu and J. T. Groves, *Med. Biol. Eng. Comput.*, 2010, **48**, 955–963.
4 B. Sorre, A. Callan-Jones, J. B. Manneville, P. Nassoy, J. F. Joanny, J. Prost, B. Goud and P. Bassereau, *Proc. Natl. Acad. Sci. U S A.*, 2009, **106**, 5622–5626.
5 H. Jia, T. Litschel, M. Heymann, H. Eto, H. G. Franquelim and P. Schwille, *Small*, 2020, **16**, 1906259.
6 J. T. Groves, N. Ulman and S. G. Boxer, *Science*, 1997, **275**, 651–653.
7 J. Zimmerberg and S. McLaughlin, *Curr. Biol.*, 2004, **14**, R250–252.
8 M. Simunovic, E. Evergren, A. Callan-Jones and P. Bassereau, *Annu. Rev. Cell Dev. Biol.*, 2019, **35**, 111–129.
9 X. Li, L. Matino, W. Zhang, L. Klausen, A. F. McGuire, C. Lubrano, W. Zhao, F. Santoro and B. Cui, *Nat. Protoc.*, 2019, **14**, 1772–1802.
10 B. R. Olden, C. R. Perez, A. L. Wilson, I. I. Cardle, Y.-S. Lin, B. Kaehr, J. A. Gustafson, M. C. Jensen and S. H. Pun, *Adv. Healthc. Mater.*, 2019, **8**, e1801188.
11 A. Kilic and F. N. Kok, *Colloids Surf., B*, 2019, **176**, 18–26.
12 A. de la Zerda, M. J. Kratochvil, N. A. Suhar and S. C. Heilshorn, *APL Bioeng.*, 2018, **2**, 021501.
13 Y. Suzuki, M. Endo and H. Sugiyama, *Nat. Commun.*, 2015, **6**, 8052.
14 E. Darley, J. K. D. Singh, N. A. Surace, S. F. J. Wickham and M. A. B. Baker, *Genes*, 2019, **10**, 1001.
15 J. Seo, S. Kim, H. H. Park and J.-M. Nam, *Small*, 2019, **15**, 1900998.
16 T.-Y. Yoon, C. Jeong, S.-W. Lee, J. H. Kim, M. C. Choi, S.-J. Kim, M. W. Kim and S.-D. Lee, *Nat. Mater.*, 2006, **5**, 281–285.
17 Y.-S. Ryu, I.-H. Lee, J.-H. Suh, S. C. Park, S. Oh, L. R. Jordan, N. J. Wittenberg, S.-H. Oh, N. L. Jeon, B. Lee, A. N. Parikh and S.-D. Lee, *Nat. Commun.*, 2014, **5**, 4507.
18 H. Eto, H. G. Franquelim, M. Heymann and P. Schwille, *Soft Matter*, 2021, **17**, 5456–5466.
19 R. Seghir and S. Arscott, *Sens. Actuators, A*, 2015, **230**, 33–39.
20 L. Stubbington, M. Arroyo and M. Staykova, *Soft Matter*, 2017, **13**, 181–186.
21 A. H. Lippert, I. B. Dimov, A. K. Winkel, J. Humphrey, J. McColl, K. Y. Chen, A. M. Santos, E. Jenkins, K. Franze, S. J. Davis and D. Klenerman, *Biophys. J.*, 2021, **120**, 35–45.

22 R. N. Palchesko, L. Zhang, Y. Sun and A. W. Feinberg, *AW, PLoS One*, 2012, **7**, e51499.
23 Alexander X. Cartagena-Rivera, Jeremy S. Logue, Clare M. Waterman and Richard S. Chadwick, *Biophys. J.*, 2016, **110**, 2528–2539.
24 V. M. Laurent, S. Kasas, A. Yersin, T. E. Schäffer, S. Catsicas, G. Dietler, A. B. Verkhovsky and J.-J. Meister, *Biophys. J.*, 2005, **89**, 667–675.
25 H. van Hoorn, R. Harkes, E. M. Spiesz, C. Storm, D. van Noort, B. Ladoux and T. Schmidt, *Nano Lett.*, 2014, **14**, 4257–4262.
26 R. S. Petruzielo, F. A. Heberle, P. Drazba, J. Katsaras and G. W. Feigenson, *Biochim. Biophys. Acta, Biomembr.*, 2013, **1828**, 1302–1313.
27 M. Rinaldin, P. Fonda, L. Giomi and D. J. Kraft, *Soft Matter*, 2020, **16**, 4932–4940.
28 **https://www.nanoscribe.com/en/products/ip-photoresins/ip-pdms/**.
29 E. J. Miller, K. Voïtchovsky and M. Staykova, *Nanoscale*, 2018, **10**, 16332–16342.
30 J. A. Goodchild, D. L. Walsh, H. Laurent and S. D. Connell, *Langmuir*, 2023, **39**, 10843–10854.
31 M. Rinaldin, R. W. Verweij, I. Chakraborty and D. J. Kraft, *Soft Matter*, 2019, **15**, 1345–1360.
32 H. Lee and R. G. Larson, *Biomacromolecules*, 2016, **17**, 1757–1765.
33 T. Yamamoto, Y. Teramura, T. Itagaki, Y. Arima and H. Iwata, *Sci. Technol. Adv. Mater.*, 2016, **17**, 677–684.
34 R. Glazier and K. Salaita, *Biochim. Biophys. Acta, Biomembr.*, 2017, **1859**, 1465–1482.
35 D. Afanasenkau and A. Offenhäusser, *Langmuir*, 2012, **28**, 13387–13394.
36 S. Mornet, O. Lambert, E. Duguet and A. Brisson, *Nano Lett.*, 2005, **5**, 281–285.
37 P. Fonda, S. C. Al-Izzi, L. Giomi and M. S. Turner, *Phys. Rev. Lett.*, 2020, **125**, 188002.
38 M. Renner, Y. Domanov, F. Sandrin, I. Izeddin, P. Bassereau and A. Triller, *PLoS One*, 2011, **6**, e25731.
39 A. Brünger, R. Peters and K. Schulten, *J. Chem. Phys.*, 1985, **82**, 2147–2160.
40 B. M. Aizenbud and N. D. Gershon, *Biophys. J.*, 1982, **38**, 287–293.
41 I. F. Sbalzarini, A. Hayer, A. Helenius and P. Koumoutsakos, *Biophys. J.*, 2006, **90**, 878–885.
42 D. Axelrod, D. E. Koppel, J. Schlessinger, E. Elson and W. W. Webb, *Biophys. J.*, 1976, **16**, 1055–1069.
43 S. Paquay and R. Kusters, *Biophys. J.*, 2016, **110**, 1226–1233.
44 R. Parthasarathy, C. H. Yu and J. T. Groves, *Langmuir*, 2006, **22**, 5095–5099.
45 M. Rinaldin, P. Fonda, L. Giomi and D. J. Kraft, *Nat. Commun.*, 2020, **11**, 4314.
46 A. B. Subramaniam, S. Lecuyer, K. S. Ramamurthi, R. Losick and H. A. Stone, *Adv. Mater.*, 2010, **22**, 2142–2147.
47 S. L. Veatch and S. L. Keller, *Phys. Rev. Lett.*, 2002, **89**, 268101.
48 J. A. Goodchild, D. L. Walsh and S. D. Connell, *Langmuir*, 2019, **35**, 15352–15363.
49 T. Baumgart, S. T. Hess and W. W. Webb, *Nature*, 2003, **425**, 821–824.
50 C. Madwar, G. Gopalakrishnan and R. B. Lennox, *Langmuir*, 2015, **31**, 4704–4712.
51 M. M. Kozlov and J. W. Taraska, *Nat. Rev. Mol. Cell Biol.*, 2023, **24**, 63–78.

